Journal of Magnetism and Magnetic Materials 493 (2020) 165718

Contents lists available at ScienceDirect

Journal of Magnetism and Magnetic Materials

journal homepage: www.elsevier.com/locate/jmmm

Research articles

Electro-infiltrated nickel/iron-oxide and permalloy/iron-oxide nanocomposites for integrated power inductors

Connor S. Smith[a,*], Shehaab Savliwala[b], Sara C. Mills[c], Jennifer S. Andrew[c], Carlos Rinaldi[b,d], David P. Arnold[a]

[a] Department of Electrical and Computer Engineering, Gainesville, FL 32611, USA
[b] Department of Chemical Engineering, Gainesville, FL 32611, USA
[c] Department of Material Science and Engineering, Gainesville, FL 32611, USA
[d] J. Crayton Pruitt Family Department of Biomedical Engineering, Gainesville, FL 32611, USA

ARTICLE INFO

Keywords:
Soft magnetic materials
Electroplating
Magnetic nanocomposites
Magnetic nanoparticles
Power electronics

ABSTRACT

Magnetic nanocomposite materials are of interest for applications including power inductors and transformers, where a combined large bandwidth, low loss, and relatively high permeability are desired. This work demonstrates the fabrication of nickel/iron-oxide nanocomposites, up to ~3 μm thick, and permalloy/iron-oxide nanocomposites, up to ~1 μm thick, using an electro-infiltration process, whereby the voids in an iron-oxide nanoparticle film are filled with electroplated metal. Measurements show that the magnetic nanocomposites exhibit hybrid magnetic properties: modestly high permeability and saturation attributed to the metal matrix phase, but with an increased bandwidth attributed to the iron-oxide inclusion phase. At 10 MHz, the nickel/iron-oxide nanocomposite material exhibits a relative permeability of ~23, with a loss tangent around 0.1; the permalloy/iron-oxide nanocomposite exhibits a relative permeability of ~136, with a loss tangent around 0.15.

1. Introduction

Magnetic nanocomposites have great potential for improving the power density and efficiency of compact power electronic devices by providing a relatively high permeability at high frequencies with low losses [24,25]. Specifically, the need for high permeability is critical for devices such as power microinductors, which see an increase in inductance with an increase in permeability of their core materials. Operating such inductors at higher frequencies is also desirable, as their power handling increases with frequency, as seen by $P_{max} = V_{core} f_{sw} B_s^2/2\mu$, where P_{max} is the maximum power handling capacity of the inductor, V_{core} is the volume of the core, f_{sw} is the switching frequency, B_s is the saturation magnetization, and μ is the magnetic permeability [21]. However, traditional microfabricated magnetic core materials usually see both a decrease in permeability and high losses at higher frequencies, so an extension of the operating bandwidth of magnetic core materials is of great interest [9].

A magnetic nanocomposite comprises two different material phases where at least one of the phases has a characteristic length scale of ~100 nm. The typical goal of a magnetic nanocomposite is to achieve a combination of desirable electromagnetic properties that are otherwise unachievable using single-phase materials. Simple nanocomposite multilayers (2–2 connectivity) are commonly fabricated using sputtering or other thin-film deposition techniques [17,16,15,18,5,19,35]. More complex composites with 0–3 or 1–3 connectivities are more difficult to microfabricate. However, magnetic nanocomposites composed of a nanoparticle phase and a metal matrix phase have been made via cluster deposition [1,12] and magnetic composite electroplating [7,8]. These techniques are plagued by either expensive deposition tools (as seen in the cluster deposition method), or low particle fill ratios (< 5%) (as seen in the composite electroplating method), resulting in nanocomposites that are less attractive for applications. However, the method of electro-infiltration, developed by Wen et al. and Hayashi et al., has shown promise as a path to creating magnetic nanocomposites in a cost-effective manner and with much higher fill ratios (~60%) [10,33,32,31].

In this work, electro-infiltration was used to fabricate two different magnetic nanocomposite materials: one composed of iron-oxide nanoparticles (IONs) embedded in a nickel matrix, and the other composed of IONs embedded in a Ni-Fe matrix (the target composition was $Ni_{80}Fe_{20}$, and hereafter is referred to as “NiFe” or “permalloy”). The structure of these composites was examined using scanning electron microscopy (SEM) and energy dispersive spectroscopy (EDS), which help confirm that the IONs have been properly embedded in the

* Corresponding author.
E-mail address: connor.smith@ufl.edu (C.S. Smith).

https://doi.org/10.1016/j.jmmm.2019.165718
Received 19 April 2019; Received in revised form 15 July 2019; Accepted 17 August 2019
Available online 24 August 2019

electroplated metals. Vibrating sample magnetometry (VSM) was used to measure the dc magnetic characteristics to determine if the composite acts as a hybrid of its components by showing a magnetic saturation and coercivity between those of the components. Finally, an Agilent E4991A Material Analyzer was used to measure the complex permeability spectra of the composite and its constituent phases to investigate permeability and loss characteristics for potential applications in power electronics.

2. Materials and methods

2.1. Iron-oxide nanoparticles

Iron oxide nanoparticles were synthesized using a two-step semi-batch thermal decomposition method developed by Vreeland et al. [29]. First, a stable, stoichiometrically defined precursor iron (III) oleate was synthesized, via a high temperature (320 °C) displacement reaction between iron acetylacetonate and a stoichiometric excess of oleic acid (1:5 Fe: oleic acid molar ratio). For this, 20.53 g of $Fe(acac)^3$ and 80.2 g of oleic acid were charged to a 500 ml round bottom reactor with continuous stirring at 350 rpm. A condenser was used to set up reflux in the system, as well as control the rate of off-gassing of the system. The reactor was immersed in a molten metal bath and heated to 320 °C using an underdamped PID control profile to prevent overshoot. Reaction endpoint was determined in previous experiments via FTIR analysis to be 35 mins after the reactor temperature crossed 300 °C. At this point, the reactor was cooled by raising it out of the molten metal and product was cooled under inert (argon) flow. The iron (III) oleate with 35–37% free oleic acid, and bridging coordination, was stored in sealed vials at room temperature.

Next, we used a semi-batch thermal decomposition reaction to synthesize a monodisperse population of iron oxide nanoparticles [28,29]. Briefly, an iron oleate with 35–37% free oleic acid and bridging coordination was diluted in 1-octadecene to 0.22 M, and added at a continuous flowrate of 12 ml/hr to a mixture of 10.03 g docosane and 6.23 g oleic acid (20 ml of initial reaction volume) in a round bottom reactor. The mixture was stirred continuously (via overhead stirring) at 350 rpm, while immersed in a molten metal bath soaking at 350 °C. The precursor drip was stopped at 5 h of reaction time, and the reaction was stopped by raising the reactor out of the molten metal. The product was recovered once cooled down.

The nanoparticles were purified from the excess reactants using antisolvent precipitation. Hexane was added to the crude product in a 1:1 volume ratio and sonicated for 10 min to disperse the nanoparticles in solution. Acetone was then added in a 1:1 acetone: suspension ratio, and the mixture was centrifuged at 2000 rcf to precipitate the oleic acid coated nanoparticles. The supernatant, containing most of the organics, was decanted, and particles were allowed to dry in air for a day before resuspending in hexane at a 10 mg/ml concentration. Finally, the particles were phase transferred to water by means of an oxidative cleavage of the double bond in oleic acid chains to give azelaic acid. Using a procedure adapted from Wang et al., sodium periodate was added to a mixture of the particles suspended in hexane, acetonitrile, ethyl acetate and water in a 1:0.5:0.5:1 ratio [30]. The mixture was sonicated for 1 h till the particles were observed to have transferred to the aqueous layer, then precipitated using a strong magnet placed underneath the container. The particles were rinsed of excess oxidizer using multiple washes with water and ethanol, then suspended in water after drying in air for a day.

The physical size distribution of the nanoparticles was characterized using images taken on a 100 kV Hitachi H7000 TEM. Purified particles were placed on a formvar-coated Cu mesh grid for imaging. Micrographs were analyzed using an open-source image analysis software called ImageJ, using at least 1000 particle diameters to fit the particles diameters to a lognormal distribution [22]. The number median physical diameter and polydispersity were calculated from the same. The particles were then suspended in toluene and equilibrium magnetization measurements were obtained at 300 K on a SQUID MPMS 3 (Quantum Design) between −7 T to 7 T. The magnetization data was fitted using a Langevin-Chantrell to obtain a volume-weighted distribution of magnetic diameters for the particle suspension [4,14,26]. Igor Pro 6.3.7 was the program used to perform the regression.

X-ray diffraction patterns were collected using a Panalytical X'pert powder diffractometer with a Cu anode (Kα radiation) and scintillation detector (45 kV, 40 mA). The iron oxide nanoparticle sample was scanned with a step size of 0.008°. The phase of the particles was then determined via comparison to database patterns from the International Center for Diffraction Data (ICDD), with the following ID number for magnetite – 98-004-4525. Scherrer's formula, $\tau = k\lambda/\beta\cos\theta$, was then used to calculate the crystallite size of the particles. Here, τ is the mean crystallite size, k is the shape factor (assumed to be 0.9 for spherical particles), λ is the X-ray wavelength (1.54 Å), β is the full width half maximum value in radians, and θ is the Bragg angle.

2.2. Magnetic nanocomposites

Electro-infiltration was used to microfabricate the nanocomposite structures, as developed and described by Wen et al. [33]. As seen in Fig. 1, magnetic nanoparticles are drop-cast into molds formed on a silicon substrate, which are then dried in air at room temperature to form a porous particle film layer. Then, these molds are placed into an electroplating bath to infiltrate and fill the porous particle films with a metal matrix and form a composite material. Compared to previous work [33], the main modification to the electro-infiltration technique here is the addition of a retaining magnet held near the backside of the particle mold sample during electroplating, which is believed to help hold the magnetic nanoparticles in place as opposed to falling off into the bath. In some samples, the particles will stay in place in the mold during plating, but more consistently, without the retaining magnet in place, particles are visually seen to fall off in small (about < 0.5 mm) pieces. Finally, the molds on the silicon substrate are removed, leaving a composite magnetic material behind. Further details of this process are explained below.

The modified electro-infiltration process begins with (100) p-type silicon substrate that was sputtered with a 20 nm titanium adhesion layer and a 100 nm gold layer, which acts as an electrode for the electroplating processing and has a low propensity to oxidize. These metals were dc sputtered using a KJL CMS-18 Multi-Source sputtering tool. Subsequently, an 11.4-μm-thick layer of AZ-9260 (MicroChem GmbH) positive photoresist was patterned into an array of mold shapes consisting of both 5 mm diameter circles and 5 mm × 5 mm squares. Due to limited space in the electroplating setup used, the wafer was then diced into smaller pieces each containing one of the circular or square molds.

The particle solution of IONs were drop-cast into the sample molds, and allowed to dry over the course of 1–2 h. For both the circular and square samples, roughly 35 μL of particle solution was required to fill the mold, as measured using a 10–100 μL micropipette. For samples to be infiltrated with nickel, a nickel sulfamate bath from Technic Inc. (Technic Nickel "S") was used. The bath is placed on a magnetic stirrer with a hotplate and heated to a temperature of 54 °C while being mixed at a stirring rate of 60 rpm using a 1 cm long magnetic stir rod. This low stir rate was chosen to lessen any agitation the particles might experience while in the plating bath. A benchtop power supply was used to deliver a constant current density of 10 mA/cm^2 between the nickel anode and particle sample mold. A NdFeB permanent magnet is placed roughly 1 cm behind the sample, outside the beaker. This magnet is kept in place for the entire plating and moved out of position whenever the sample is removed from the bath. For samples to be infiltrated with permalloy, a permalloy bath was used, with the bath recipe listed in Table 1. The temperature of this bath was kept at 25 °C without any

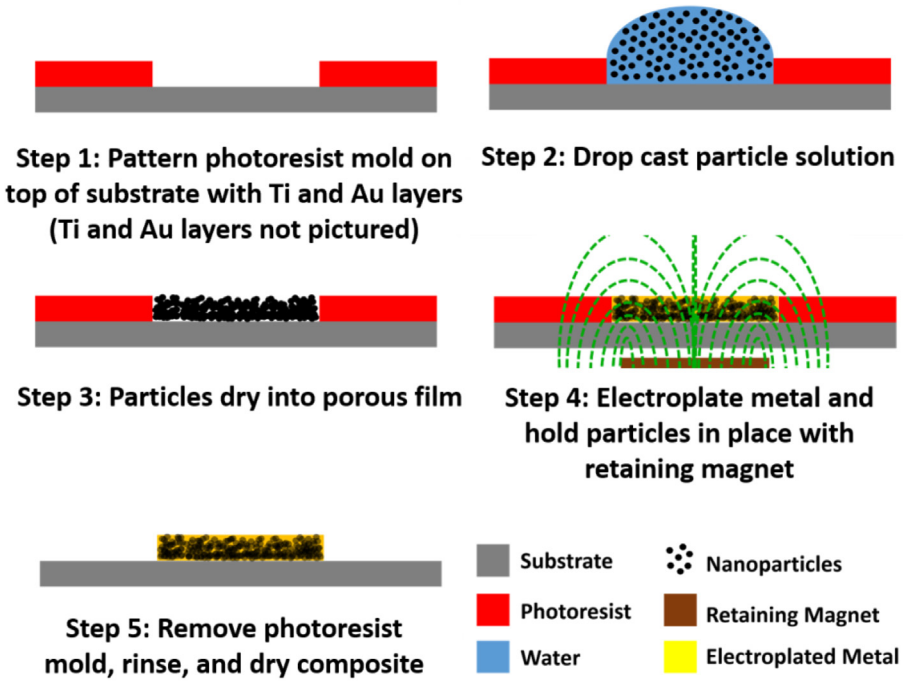

Fig. 1. Enhanced electro-infiltration process, which includes a retaining magnet used during the electroplating step to hold nanoparticles in place. Step 1 shows the initial substrate that has been sputtered with Ti and Au (layers not shown), as well as patterned into a mold with photoresist. Step 2 shows the drop casting of particle solution on the molds, which then dry into a porous particle film as seen in Step 3. Step 4 illustrates the enhanced electro-infiltration process, where a retaining magnet is used to hold the particles in place in the mold while a metal is electroplated through the particle film. Step 5 provides the final result of this process after removing the photoresist mold—a composite electroplated metal and particle material.

Table 1
Recipe for permalloy electroplating bath.

Chemical	Concentration
nickel(II) sulfate (NiSO4.6H2O)	200.0 g/L
nickel(II) chloride (NiCl2.6H2O)	5.0 g/L
iron(II) sulfate (FeSO4.7H2O)	8.0 g/L
boric acid (H3BO3) Powder	25.0 g/L
saccharin (C7H5NO3S)	3.0 g/L

agitation during the plating, with an applied current density of 10 mA/cm^2 between the nickel anode and particle sample mold. Following infiltration, the photoresist molds are removed by soaking the samples in acetone, rinsing with water, and then drying under a stream of air.

Like the particles, X-ray diffraction patterns of the composites were collected using a Panalytical X'pert powder diffractometer with a Cu anode (Kα radiation) and scintillation detector (45 kV, 40 mA). The composite samples were scanned with a step size of 0.016°, with a 5° omega offset, and a fixed irradiated length of 6 mm. This offset was applied to avoid damage to the detector from the single crystal silicon substrate. The phase of each individual constituent was then determined via comparison to database patterns from the International Center for Diffraction Data (ICDD), with crystallite sizes of the Ni and NiFe phases calculated using Scherrer's formula. Diffraction data ID numbers were as follows: gold – 98-004-4362, magnetite – 98-004-4525, nickel – 98-007-6667, and nickel-iron – 98-010-3559.

Permeability measurements using the Agilent 4991A Material Analyzer with 16454A Magnetic Material Test Head required a toroidal sample of the composite that has an outer diameter ≤8 mm, an inner diameter ≥3.1 mm, and a thickness ≤3 mm. As fabricating such a shape on a silicon substrate would be difficult due to the need to ultimately cut out the toroid for measurement, these structures were instead fabricated on top of an aluminum foil substrate that could be easily cut. This substrate was made by taking a piece of store-bought aluminum foil (~24 μm thick), and wrapping it around a glass slide to provide a flat and stable surface to work on. This foil-wrapped slide was then put through the same fabrication process as described for the silicon substrate above, with the toroidal shape patterned onto the substrate using a photolithography mask. Finally, after the material to be measured was deposited, the foil was unwrapped from the glass slide, and the toroidal shape was cut out of the foil using scissors and a hole punch of appropriate size. An example of a fabricated toroidal sample can be seen in the stereoscope image of Fig. 2.

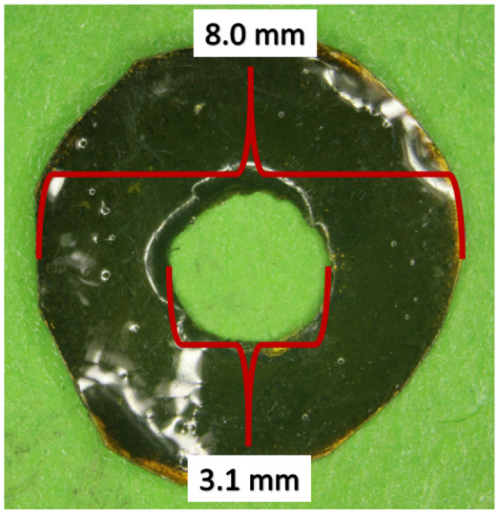

Fig. 2. Stereoscope image of an example toroidal composite sample fabricated on, and cut out from, aluminum foil. Note that glare is from a piece of Kapton tape used to cover and protect composite film. This sample geometry is necessary for measurement of the complex permeability of the materials using the Agilent 16454A Magnetic Material Test Head.

For compositional characterization, composite samples were cross-sectioned and examined using a FEI Nova 430 SEM with EDS capabilities, in order to view the composite structure and composition. EDS was also performed in order to determine if there was a presence of both electroplated metal (Ni or NiFe) alongside the IONs in the infiltrated material cross-sections. For magnetic characterization, samples were characterized using an ADE Tech. EV-9 VSM with max fields of 1800 kA/m to measure and plot their hysteresis loops. Finally, complex permeability measurements were taken using an Agilent 4991A Material Analyzer with a 16454A Magnetic Material Test Head using

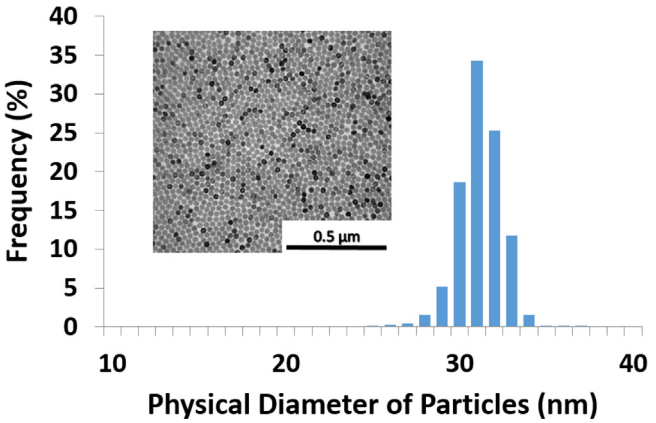

Fig. 3. Histogram of the physical diameter size distribution of the fabricated IONs. Inset to the figure is a TEM image of the IONs. Note the narrow size distribution of the particle diameters, with a peak at 31 nm. The TEM image also shows good uniformity of the size of the particles, as well as of their spherical shape.

the toroidal test samples. The measurements were taken under no dc bias, and with an ac field of ~0.3 A/m (a maximum oscillating current of 10.04 mA was supplied). The real and imaginary parts of the complex impedance were used with the dimensions of the toroid sample to calculate the real permeability by $\mu' = 1 + (X_S - X_{air})/\mu_0 \hat{A} \cdot h \hat{A} \cdot ln(b/a)$ and the imaginary permeability by $\mu'' = (R_S - R_{air})/\mu_0 \hat{A} \cdot h \hat{A} \cdot ln(b/a)$. Here, X_s is the imaginary part of the impedance when the sample is in the test head, X_{air} is the imaginary part of the impedance when the sample is not in the test head, R_s is the real part of the impedance when the sample is in the test head, R_{air} is the real part of the impedance when the sample is not in the test head, h is height of the toroid sample, b is outer radius of the toroid sample, and c is the inner radius of the toroid sample [6]. The loss tangent was calculated by dividing the imaginary part of the permeability by the real part of the permeability ($tan\delta = \mu''/\mu'$).

3. Results and discussion

3.1. Iron-oxide nanoparticles

Fig. 3 shows the physical size distribution histogram for the fabricated IONs. From this graph, it is seen that the IONs have a narrow size distribution, with a peak at 31 nm in diameter. The inset of Fig. 3 also shows a TEM image of the IONs, which support their uniform size distribution and spherical shape. From SQUID measurement and curve fitting, the magnetic diameter of these IONs was found to be 16.0 nm.

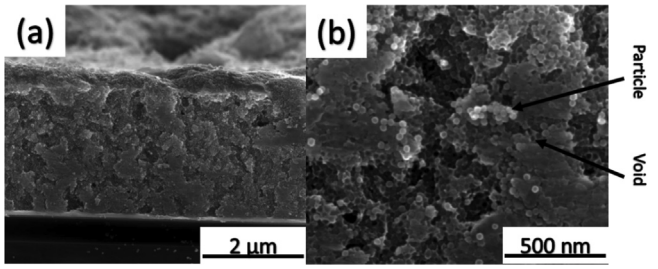

Fig. 5. SEM images of Ni/IONs composite cross-section (cleaved) at magnifications of 100000x (a) and 25000x (b). The cross-section in (a) shows how the material is infiltrated with Ni through ~3 μm of the ION film, while (b) shows a closer look at the presence of IONs in the composite, as well as the presence of voids where IONs seemingly fell off during cleaving.

Fig. 4 shows the XRD pattern of the IONs, revealing the expected characteristic peaks from the spinel crystal structure of iron oxide. From Scherrer's formula, the crystallite size of the particles was calculated to be 17.0 ± 2.2 nm. The crystallite size calculated from Scherrer's formula is comparable to the reported magnetic diameter of these IONs, 16.0 nm, validating the measurement of the crystallite size.

3.2. Nickel/iron-oxide nanoparticle composite

Fig. 5 shows SEM images of the cleaved cross-section of the Ni/IONs nanocomposite with a thickness of ~3 μm. Fig. 5a shows an image of the particles themselves, surrounded by a matrix of nickel metal. An example of a particle in the matrix, and a void left behind by a particle that fell off during cleaving, are noted. Fig. 5b shows how the particle and nickel composite is uniformly structured across the height of the cross-section. Fig. 6 shows an EDS mapping of the Ni/IONs composite cross-section. In this mapping of the composite, the two elements, Ni and Fe (presumed to be from the IONs) are seen to be spread out across the whole cross-section, suggesting uniformity of the structure

3.3. Permalloy/iron-oxide nanoparticle composite

Fig. 7 shows SEM images of the cleaved cross-section of the NiFe/IONs nanocomposite with a thickness of ~1 μm. Fig. 7a shows an image of the particles themselves, surrounded by a matrix of permalloy metal. An example of a particle in the matrix, and a void left behind by a particle that fell off during cleaving, are noted. Fig. 7b shows how the particle and permalloy composite is uniformly structured across the height of the cross-section. Note the presence of un-infiltrated particles left on top of the composite, which make up the part of the particle film that was not infiltrated during electroplating due to prematurely ending the electroplating step. These particles were kept on the SEM sample for

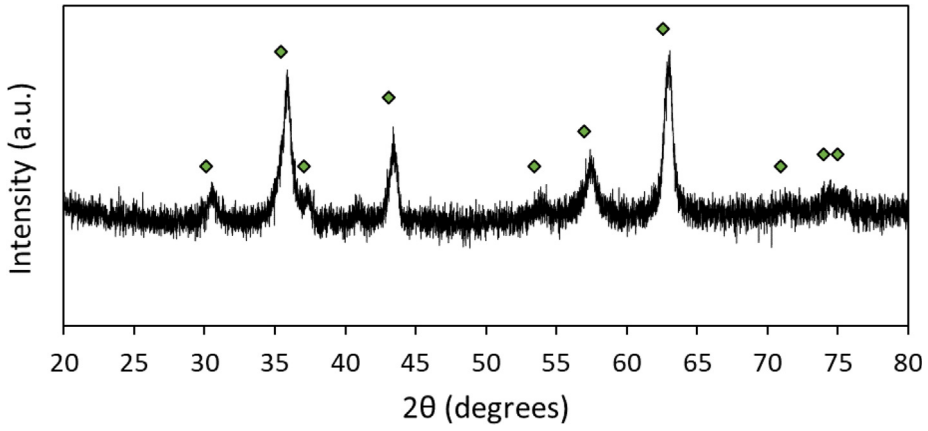

Fig. 4. XRD pattern of the IONs used in the composites. Diamonds represent the peaks from a reference pattern of magnetite, with ID number 98-004-4525.

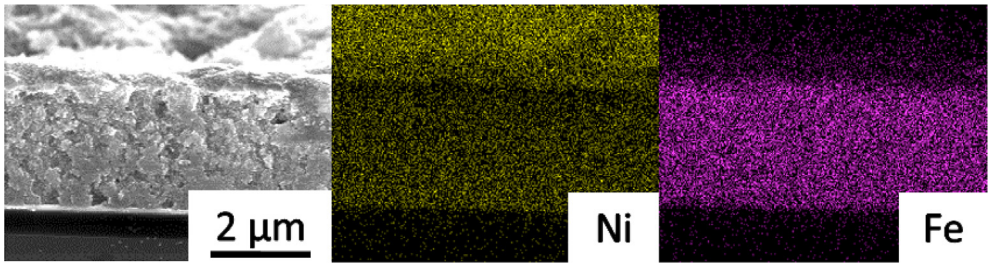

Fig. 6. EDS mapping for nickel and iron of the cross-section of the Ni/IONs composite sample. Note the presence of both Ni and Fe (presumedly from the IONs) that are uniformly dispersed throughout the cross-section of the composite—indicating a successful infiltration of Ni through the ION film.

demonstration of how the non-infiltrated particle layer looks, but these un-infiltrated particles were removed via rinsing with DI water on samples used to measure magnetic properties. Fig. 8 shows an EDS mapping of the NiFe/IONs composite cross-section. In this mapping of the composite, the two elements, Ni and Fe (presumed to be from both the NiFe and the IONs) are seen to be spread out across the whole cross-section, suggesting uniformity of the structure. The presence of iron in the un-infiltrated particle layer suggests that this region of the particle film was not infiltrated.

3.4. Comparison of magnetic composites

Fig. 9 shows the XRD patterns of the Ni/IONs, NiFe/IONs, and IONs. Each composite was then compared to the appropriate reference material. The diffraction pattern of the Ni/IONs composite exhibits the characteristic peaks of face cubic centred (FCC) nickel, spinel iron oxide, and FCC gold. Similarly, the diffraction pattern of the NiFe/IONs composite indicates the presence of both the inclusion phase of spinel iron oxide nanoparticles and the electroinfiltrated FCC nickel iron matrix, along with that of FCC gold. Each composite's diffraction pattern contains FCC gold peaks from the underlying gold seed layer. The gold peaks in the NiFe/ION pattern are of much higher intensity however, likely due to the thinner size of this sample as compared to the Ni/ION composite. Using Scherrer's formula, the size of the crystallites of the Ni and NiFe matrix phases in each respective composite was calculated. By Scherrer's formula, the Ni crystallites in the Ni/IONs composite were calculated to be 23 nm, while those crystallites of NiFe in the NiFe/IONs composite measured 12 nm.

Fig. 10 compares the hysteresis curves of the composite materials with that of each of their constituents—the metal matrices and the IONs. Table 2 provides the magnetic parameter values for the various materials as extracted from their hysteresis curves. The Ni/IONs composite material is seen to have a saturation magnetization of 447 kA/m, which lies between those of the nickel (513 kA/m) and the ION (385 kA/m) bare samples. Similarly, the NiFe/IONs composite material is seen to have a saturation magnetization of 668 kA/m, which lies between those of the permalloy (925 kA/m) and the ION (385 kA/m) bare samples. This result demonstrates that the saturation magnetization of the composite materials are a hybrid of their constituent parts, as suggested by previous work [33,32]. A kink-free hysteresis curve for the composites also gives evidence of exchange coupling between the two phases, as opposed to a simple superposition of the hysteresis curves.

The complex permeability curves and loss tangent (tanδ) are compared in Fig. 11. As seen in Fig. 11a and d, the real part of the permeability of the composites retains the relatively larger bandwidth of the IONs, going up to 10 MHz, while still retaining a relatively high permeability around 23 (for the Ni/IONs composite) and 136 (for the NiFe/IONs composite), as provided by their respective metal matrices. Fig. 11c and 11f show the composites also maintain a loss tangent around 0.1 at and below 10 MHz (for the Ni/IONs composite) and around 0.15 at and below 10 MHz (for the NiFe/IONs composite), as Fig. 11b and 11e show they both approach their ferromagnetic resonance (FMR) peaks seen at about 80 MHz and 100 MHz, respectively. The FMR peaks for the nickel and the IONs are both lower than 1 MHz, and are thus not visible in these plots [2,34]. Further, the permalloy FMR peak appears around 2 MHz, with such a low FMR expected in thicker films [11,27]. Both composite materials show improved performance as compared to the metals and IONs, as they both maintain low losses at 10 MHz, while maintaining a high permeability. In comparison, the nickel and IONs both provide relatively higher losses and low permeabilities, while the permalloy provides a higher permeability, but also higher losses. These results show that these composite materials could be used in a device operating at or below 10 MHz, where a stable and relatively high permeability could be provided along with low losses, as compared to the metal and IONs alone.

Fig. 12 shows a plot comparing the critical magnetic material parameters necessary for the design of devices such as inductors—the permeability and the loss tangent. From Fig. 11, it is seen that 10 MHz appears to be the maximum optimal operating frequency of the composite materials as their loss tangents are both at a minimum, so values at this frequency were used in Fig. 12. Alongside the material analyzed in this work, other results from the literature on magnetic nanocomposites and soft magnetic materials are listed as well. The selection of results to include were based on whether or not data was given on the permeability and loss tangent of the materials at 10 MHz.

The materials fabricated in this work show an improved performance of that of their constituent parts, and are comparable to other

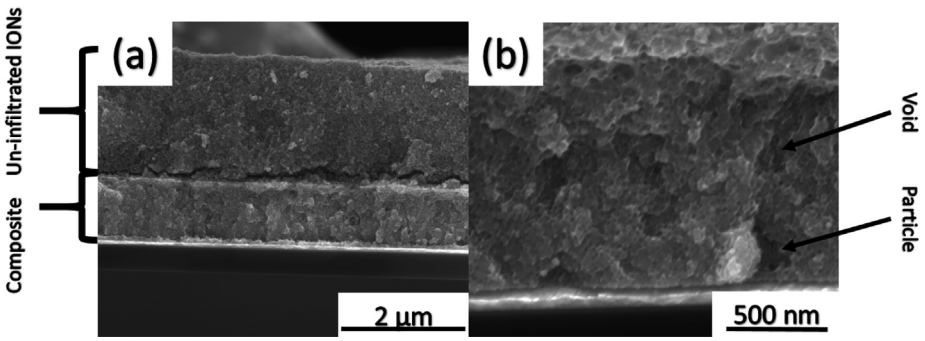

Fig. 7. SEM images of NiFe/IONs composite cross-section (cleaved) at magnifications of 160000x (a) and 20000x (b). The cross-section in (a) shows how the material is infiltrated with NiFe through ~1 μm of the ION film, while (b) shows a closer look at the presence of IONs in the composite, as well as the presence of voids where IONs seemingly fell off during cleaving.

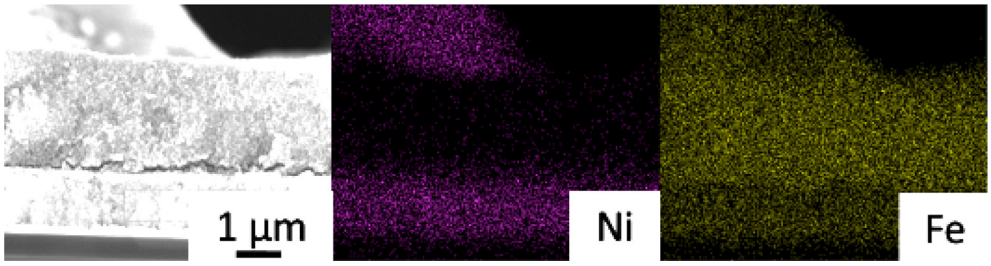

Fig. 8. EDS mapping for nickel and iron of the cross-section of the NiFe/IONs composite sample. Note the presence of both Ni (presumably from the NiFe) and Fe (presumably from the IONs and NiFe) that are uniformly dispersed throughout the cross-section of the composite—indicating a successful infiltration of NiFe through the ION film, as well as the remains of un-infiltrated IONs on top of the sample.

materials presented in the literature. Both the Ni/IONs and NiFe/IONs composites show a higher permeability than those of composites formed from a combination of magnetic particles in a polymer resin, as expected by the higher volume of magnetic materials present within them. There is a marked increase in the loss tangent of the Ni/IONs and NiFe/IONs composites as compared to many of the particle/polymer composites, which is also expected from the presence of a conductive magnetic metal (Ni or NiFe) surrounding the particles instead of an insulating polymer resin, whereby eddy current losses can arise. As mentioned, the need for high permeability is critical for devices such as power microinductors to increase their inductance. High frequency operation is also desirable, as power handling capabilities increase with frequency. However, traditional microfabricated magnetic core materials, such as nickel and permalloy, are plagued by both a decrease in permeability and high losses at higher frequencies. The above results show that both magnetic composites reported here had an extension of their operating bandwidth, with high permeability and low losses extending up to about 10 MHz before decreasing and increasing, respectively. In conclusion, there is a marked improvement in the permeability of the composites in of this work compared to those made from polymer/particle mixtures and composite particles (> 10), and an improvement in their loss tangents compared to their constituent parts (< 1). There is still room for improvement in terms of both permeability and loss tangent in comparison to bulk materials from companies such as the Fair-Rite Corporation, however the ability to scale the microfabrication of composite materials using electro-infiltration allows for their use in a myriad of applications such as in micro-inductors and other on-chip power electronics.

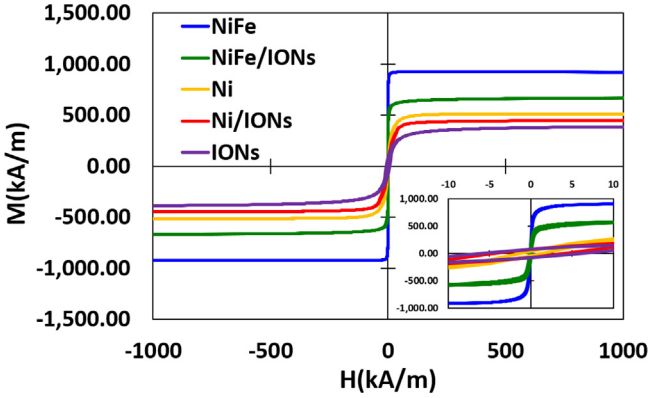

Fig. 10. Hysteresis curve of the magnetic composites (Ni/IONs and NiFe/IONs) compared against the hysteresis curves of the constituent pure materials: nickel (Ni), permalloy (NiFe) and iron-oxide nanoparticles. Inset: Zoom-in to the center of the hysteresis curves. Note that the saturation magnetization of the composite materials falls between the saturation magnetization of each of its constituent parts, indicating an averaging of the two material properties.

4. Conclusion

The work presented here expands upon the electro-infiltration process for making magnetic nanocomposite materials made from magnetic nanoparticles and surrounding metal matrices. Compared to prior publications on electro-infiltration, the introduction of a retaining magnet into the process has allowed for more consistent results when fabricating these nanocomposites, by keeping the magnetic nanoparticles in place in the mold during electroplating. The magnetic behavior and characterization of the metal and iron oxide nanoparticle composites, as seen throughout this work, show promise towards the fabrication of devices such as power microinductors, which rely upon microfabricated magnetic materials with high permeability and low losses, while operating at frequencies in the range of 10 kHz to 300 MHz [25]. The composite materials explored show that they are capable of retaining the high permeability (~110 for 99% pure Ni, and ~8000 for 78 NiFe) [3] of their metal matrix phase, as well as see an expansion of their bandwidths to 10 MHz upon the addition of their particle phase. In

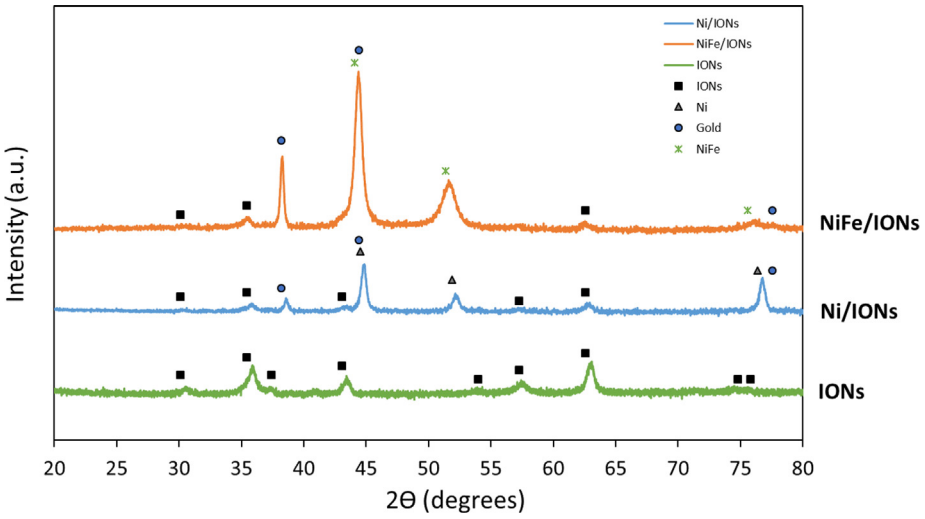

Fig. 9. XRD patterns of the composites, Ni/IONs and NiFe/IONs, and IONs only compared with the appropriate reference pattern for each material: square (IONs), triangle (Ni), asterisk (NiFe), and circle (gold), with ID numbers as follows: gold – 98-004-4362, magnetite – 98-004-4525, Ni – 98-007-6667, and NiFe – 98-010-3559.

Table 2
Magnetic parameters extracted from material hysteresis curves.

Parameter	Ni	NiFe	IONs	Ni/IONs	NiFe/IONs
Saturation Magnetization (M_s)	513 kA/m	925 kA/m	385 kA/m	447 kA/m	668 kA/m
Magnetic Remanence (M_r)	40.6 kA/m	130 kA/m	81.6 kA/m	79.1 kA/m	145 kA/m
Coercivity (H_c)	2.43 kA/m	0.08 kA/m	7.36 kA/m	2.43 kA/m	0.08 kA/m
Squareness (M_r/M_s)	0.08	0.14	0.21	0.18	0.22

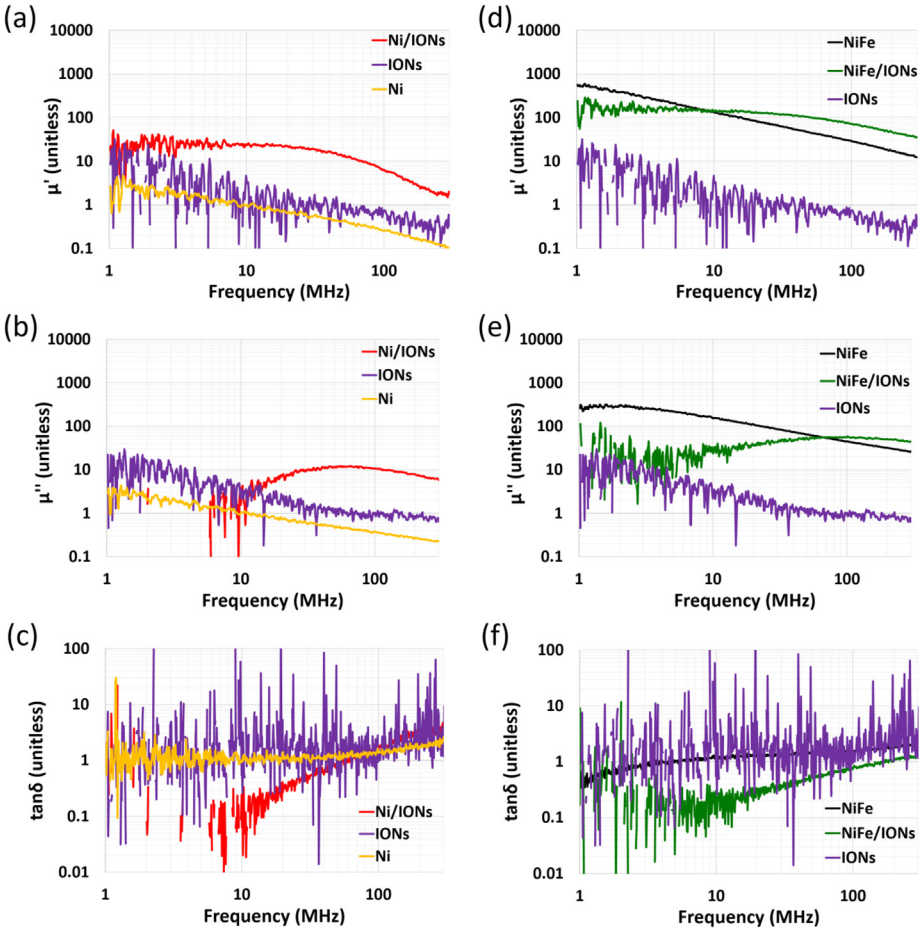

Fig. 11. Permeability spectra for the various samples, specifically the (a) real permeability, (b) imaginary permeability, and (c) loss tangent for the Ni/IONs composite, nickel, and IONs; and (d) real permeability, (e) imaginary permeability, and (f) loss tangent for the NiFe/IONs composite, permalloy, and IONs. Note that both the composite materials appear to have an extended bandwidth than either of their constituent parts, whereby the permeability of both composites is constant up to about 10 MHz. Note that both composites also show a reduced loss tangent compared to their constituent parts, with a minimum appearing around 10 MHz.

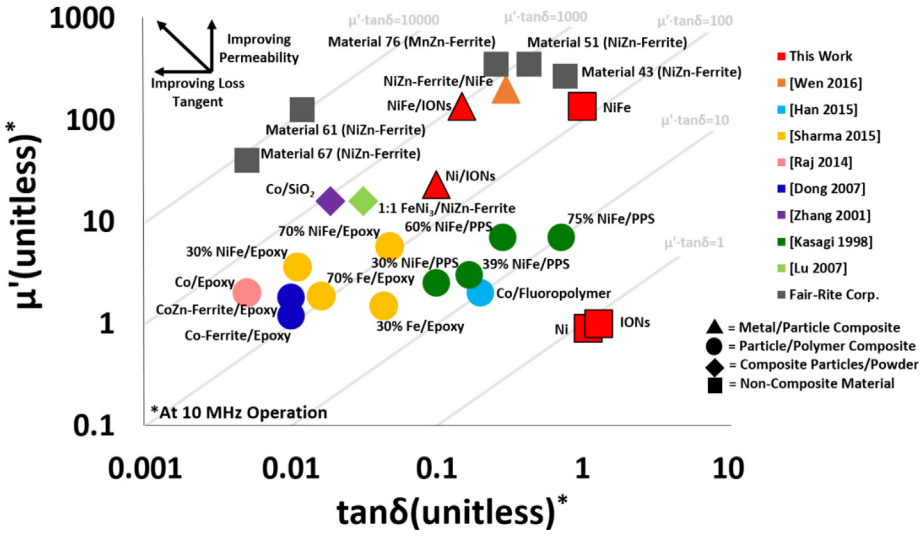

Fig. 12. A comparison plot of the critical magnetic material characteristics necessary for inductor design—the permeability and the loss tangent. These values were taken at 10 MHz, which is the maximum optimal operating point of the composite materials as seen in Fig. 9. Materials from both this work and other literature have been included. Note that the materials characterized in this work (shown in red with a black border) have a higher permeability than many of the materials shown that are made from composites using polymer matrices (shown as circles), but also experience a higher loss tangent, likely due to the presence of a conductive metal matrix. (See above-mentioned references for further information.) (For interpretation of the references to colour in this figure legend, the reader is referred to the web version of this article.)

comparison to magnetic composites manufactured through other means (as seen in Fig. 12), the composites in this work achieve higher permeabilties (> 10) at 10 MHz than those made from polymer/particle mixtures or composite particles/powers, and lower lost tangents than those provided by their constituent parts (< 1). However, further work is still required in order to reach the performance quality of the materials made by companies such as the Fair-Rite Corporation, though the ability to scale the microfabrication of composite materials using electro-infiltration allows for more applications in on-chip power electronics. Future work will seek to improve the properties and expand on the applications of these composites, as well as the variety of composites that can be fabricated.

Acknowledgements

This work was funded in part by the National Science Foundation (CMMI-1727930). The authors thank the staff of the Herbert Wertheim College of Engineering Research Service Center at the University of Florida for assistance in the fabrication and material analysis.

References

[1] B. Balasubramanian, R. Skomski, X. Li, S.R. Valloppilly, J.E. Shield, G.C. Hadjipanayis, D.J. Sellmyer, Cluster synthesis and direct ordering of rare-earth transition-metal nanomagnets, Nano Lett. 11 (4) (2011) 1747–1752.
[2] N. Bloembergent, On the ferromagnetic resonance in nickel and supermalloy, Phys. Rev. 78 (5) (1950).
[3] W.F. Brown, Magnetic Materials, Handbook of Chemistry and Physics. McGraw-Hill, 1958.
[4] R.W. Chantrell, J. Popplewell, S.W. Charles, Measurements of particle-size distribution parameters in ferrofluids, IEEE Trans. Mag. 14 (5) (1978) 975–977.
[5] H. Dong, A. Meininger, H. Jiang, K.S. Moon, C.P. Wong, Magnetic nanocomposite for potential ultrahigh frequency microelectronic application, J. Electron. Mater. 36 (5) (2007) 593–597.
[6] R. Dosoudil, Determination of permeability from impedance measurement using vector network analyzer, JEE 63 (7) (2012) 97–101.
[7] S. Guan, B.J. Nelson, Pulse-reverse electrodeposited nanograinsized CoNiP thin films and microarrays for MEMS actuators, J. Electrochem. Soc. 152 (4) (2005) C190.
[8] S. Guan, B.J. Nelson, Magnetic composite electroplating for depositing micromagnets, J. Microelectromechanical Syst. 15 (2) (2006) 330–337.
[9] K. Han, M. Swaminathan, P. Raj, H. Sharma, R. Tummala, S. Yang, V. Nair, Magneto-dielectric nanocomposite for antenna miniturization and SAR reduction, IEEE Antenn. Wirel. Pr. 15 (2016) 72–75.
[10] Y. Hayashi, S. Hashi, K. Ishiyama, Magnetic properties of nanostructured film composed of co-ferrite nanoparticles and metal co prepared by combination of electrophoretic deposition and electroplating, IEEE Trans. Magn. 48 (11) (2012) 3170–3173.
[11] T. Kasagi, T. Tsutaoka, K. Hatakeyama, High frequency permeability of permalloy and its composite materials, J. Magn. Soc. Jpn. 22 (1998) 295–297.
[12] X. Liu, S. He, J.M. Qiu, J.P. Wang, Nanocomposite exchange-spring magnet synthesized by gas phase method: from isotropic to anisotropic, Appl. Phys. Lett. 98 (22) (2011) 96–99.
[13] X. Lu, G. Liang, Y. Zhang, W. Zhang, Synthesis of FeNi3/(Ni0.5Zn0.5)Fe2O4 nanocomposite and its high frequency complex permeability, Nanotechnology 18 (2007) 1–5.
[14] L. Maldonado-Camargo, M. Unni, C. Rinaldi, Biomedical Nanotechnology: Methods and Protocols, Springer, New York, New York, 2017.
[15] J.W. Park, M.G. Allen, Ultralow-profile micromachined power inductors with highly laminated Ni/Fe cores: application to low-megahertz DC-DC converters, IEEE Trans. Magn. 39 (5 II) (2003) 3184–3186.
[16] J.Y. Park, S.H. Han, M.G. Allen, Batch-fabricated microinductors with electroplated magnetically anisotropic and laminated alloy cores, IEEE Trans. Magn. 35 (5) (1999) 4291–4300.
[17] J.Y. Park, L.K. Lagorce, M.G. Allen, Ferrite-based integrated planar inductors and transformers fabricated at low temperature, IEEE Trans. Magn. 33 (5 PART 1) (1997) 3322–3324.
[18] P.M. Raj, P. Muthana, T.D. Xiao, L. Wan, D. Balaraman, I.R. Abothu, S. Bhattacharya, M. Swaminathan, R. Tummala, Magnetic nanocomposites for organic compatible miniaturized antennas and inductors, in: Proceedings of the International Symposium and Exhibition on Advanced Packaging Materials Processes, Properties and Interfaces, 2005.
[19] P.M. Raj, H. Sharma, S. Samtani, D. Mishra, V. Nair, R. Tummala, Magnetic losses in metal nanoparticle-insulator nanocomposites, J. Mater. Sci. Mater. Electron. 24 (9) (2013) 3448–3455.
[20] P.M. Raj, P. Chakraborti, H. Sharma, K. Han, S. Gandhi, S. Sitaraman, M. Swaminathan, R. Tummala, Tunable and miniturized RF components with nanocomposite and nanolayered dielectrics, Proc. 14th IEEE Int. Conf. Nano (2014) 27–31.
[21] P.M. Raj, H. Sharma, S. Sitaraman, D. Mishra, R. Tummala, System scaling with nanostructured power and RF components, Proc. IEEE 105 (12) (2017) 2330–2346.
[22] C.A. Schneider, W.S. Rasband, K.W. Eliceiri, NIH Image to ImageJ: 25 years of image analysis, Nature Methods 9 (7) (2012) 671–675.
[23] H. Sharma, S. Jain, P.M. Raj, K.P. Murali, R. Tummala, Magnetic and dielectric proporty studies in Fe- and NiFe-based polymer nanocomposites, J. Electron. Mater. 44 (10) (2015) 3819–3826.
[24] C.R. Sullivan, Integrating magnetics for on-chip power: Challenges and opportunities, in: Proc. Cust. Integr. Circuits Conf., no. Cicc, pp. 291–298, 2009.
[25] C.R. Sullivan, D.V. Harburg, J. Qiu, C.G. Levey, D. Yao, Integrating magnetics for on-chip power: a perspective, IEEE Trans. Power Electron. 28 (9) (2013) 4342–4353.
[26] M. Unni, A. Uhl, S. Savliwala, B.H. Savitzky, R. Dhavalikar, N. Garraud, D.P. Arnold, L.F. Kourkoutis, J.S. Andrew, C. Rinaldi, Thermal decomposition synthesis of iron oxide nanoparticles with diminished magnetic dead layer by controlled addition of oxygen, ACS Nano 11 (2) (2017) 2284–2303.
[27] A.D.C. Viegas, M.A. Correa, L. Santi, R.B. da Silva, F. Bohn, M. Carara, R.L. Sommer, Thickness dependence of the high-frequency magnetic permeability in amorphous Fe73,5Cu1Nb3Si13.5B9 thin films, J. Appl. Phys. 101 (2007) 033908.
[28] E. Vreeland, Development of Novel Synthetic Methods for Size-Tunable Synthesis of Superparamagnetic Iron Oxide Nanoparticles, University of Mexico, 2014.
[29] E.C. Vreeland, J. Watt, G.B. Schober, B.G. Hance, M.J. Austin, A.D. Price, B.D. Fellows, T.C. Monson, N.S. Hudak, L. Maldonado-camargo, A.C. Bohorquez, C. Rinaldi, D.L. Huber, Enhanced nanoparticle size control by extending LaMer's mechanism, Chem. Mater. 27 (17) (2015) 6059–6066.
[30] M. Wang, M.L. Peng, W. Cheng, Y.L. Cui, C. Chen, A novel approach for transferring oleic acid capped iron oxide nanoparticles to water phase, J. Nanosci. Technol. 11 (4) (2011) 3688–3691.
[31] X. Wen, J.S. Andrew, D.P. Arnold, Exchange-coupled hard magnetic Fe-Co/CoPt nanocomposite films fabricated by electro-infiltration, AIP Adv. 7 (5) (2017).
[32] X. Wen, S.J. Kelly, J.S. Andrew, D.P. Arnold, Nickel-zinc ferrite/permalloy (Ni0.5Zn0.5Fe2O4/Ni-Fe) soft magnetic nanocomposites fabricated by electro-infiltration, AIP Adv. 6 (5) (2016).
[33] X. Wen, J.D. Starr, J.S. Andrew, D.P. Arnold, Electro-infiltration: a method to form nanocomposite soft magnetic cores for integrated magnetic devices, J. Micromech. Microeng. 24 (10) (2014).
[34] H. Yun, X. Liu, T. Paik, D. Palanisamy, J. Kim, W.D. Vogel, A.J. Viescas, J. Chen, G.C. Papaefthymiou, J.M. Kikkawa, M.G. Allen, C.B. Murray, Size- and composition-dependent radio frequency magnetic permeability of iron oxide nanocrystals, ACS Nano 8 (12) (2014) 12323–12337.
[35] J. Zhan, C. Yang, X. Wang, Q. Fang, Z.T. Shi, Y. Yang, T.L. Ren, A. Wang, Y.H. Cheng, L.T. Liu, Stacked-spiral RF inductors with vertical nanoparticle magnetic core for radio-frequency integrated circuits in CMOS, Sensors Actuators, A Phys. (2013).
[36] Y.D. Zhang, S.H. Wang, D.T. Xiao, J.I. Budnick, W.A. Hines, Nanocomposite Co/SiO2 soft magnetic materials, IEEE Trans. Mag. 37 (4) (2001) 2275–2277.